High Energy Density Aqueous Li-Ion Flow Capacitor

Hao Liu, Libing Liao, Yi-Chun Lu, and Quan Li**

High energy density Li-ion hybrid flow capacitors are demonstrated by employing $LiMn_2O_4$ and activated carbon slurry electrodes. Compared to the existing aqueous flow electrochemical capacitors, the hybrid one exhibits much higher energy densities due to the introduction of high capacity Li-insertion materials (e.g., $LiMn_2O_4$ in the present work) as the flowable electrode with asymmetrical cell configuration. A record energy density, i.e., 23.4 W h kg^{-1} at a power of 50.0 W kg^{-1} has been achieved for aqueous flow capacitors tested at static condition reported to date. A full operational Li-ion flow capacitor tested in an intermittent-flow mode has also been demonstrated. The Li-ion hybrid flow capacitor shows great promise for high-rate grid applications.

1. Introduction

Aqueous electrochemical flow capacitors have demonstrated high power capabilities and high safety and can be fabricated at low cost.[1] These characteristics make them promising for high-rate grid applications, such as peak-shaving for renewable energy generated from solar or wind. The system usually consists of separated external reservoirs for active materials storage and a power reactor for electrochemical reaction to take place, and consequently a notable feature of the system is the adoption of flowable slurry electrodes for electrochemical energy storage. Such unique architecture enables the decoupling of energy and power capacity, allowing its flexibility and scalability for grid-energy storage.[2]

A major problem of the first generation flow electrochemical capacitors is its low energy density, due to the employment of carbon beads dispersed in aqueous electrolyte as the electrode material, which suffers from rather low capacitance of ≈90 F g^{-1} and a low working voltage window of 0.6 V.[1] Several strategies have been proposed to improve the energy density, including the introduction of additional redox-active species (e.g., soluble organic molecules[3] or soluble metal ions[4]) into the carbon slurries for overall capacitances increase and employment of asymmetric electrode configuration for working voltage window extension.[5] In addition, other materials with high specific capacitance, such as graphene nanoplatelets (≈300 F g^{-1}),[6] were also employed to make flowable slurries. These strategies are effective and an ≈1.5–3 times increase in the energy densities has been achieved (≈11–14 W h kg^{-1} at a power density of ≈50–100 W kg^{-1}).[3,5] Nevertheless, the energy densities of the flow capacitors remain unsatisfactory.

Adopting the concept of Li-ion hybrid capacitor provides another possible means to improve the energy density of the flow capacitor. Indeed high energy densities with remarkably high power densities have been demonstrated in the conventional solid electrodes when Li-ion insertion materials are incorporated.[7] Compared to other representative types of the aqueous electrochemical capacitor systems,[8] including those derived from electric double layer capacitors (EDLCs) and metal oxide-based hybrid capacitor, the aqueous Li-ion hybrid capacitor generally possesses the highest energy densities practically (Table S1, Supporting Information). They become the most promising device candidates to bridge the gap between the Li-ion batteries and EDLCs. Inspired by the demonstration in the solid systems, integrating the hybrid concept into the flow cell configuration is then expected to take advantage of all three parties—Li-ion batteries (high energy densities), supercapacitors (high power densities and long lifetimes), and flow batteries (scalability).

In the present work, we demonstrated an aqueous Li-ion hybrid flow capacitor employing $LiMn_2O_4$ (LMO) and activated carbon (AC) suspension electrodes. Herein, LMO was chosen due to its moderate capacity, excellent cycling life and rate capability, and low cost as demonstrated in aqueous Li-ion batteries.[7c,9] The introduction of the hybrid architecture and the asymmetrical electrode configuration led to improved capacity and enlarged working voltage window of the flow cell, resulting in an energy density ≈1.5 times higher than the record energy density of the aqueous flow capacitor to date. A typical LMO/AC flow capacitor tested under static condition showed a high energy density of ≈23.4 W h kg^{-1} at a power density of ≈50 W kg^{-1}. The flow Li-ion capacitors under intermittent flow operation were also demonstrated.

Dr. H. Liu
School of Science
China University of Geosciences
Beijing 100083, P. R. China
E-mail: 2014010007@cugb.edu.cn
Dr. H. Liu, Prof. Q. Li
Department of Physics
Chinese University of Hong Kong, Hong Kong
E-mail: liquan@phy.cuhk.edu.hk
Dr. H. Liu
Beijing Key Laboratory of Optical Detection Technology for Oil and Gas
China University of Petroleum
Beijing 102249, P. R. China
Prof. L. B. Liao
School of Materials Science and Technology
China University of Geosciences
Beijing 100083, P. R. China
Prof. Y.-C. Lu
Department of Mechanical and Automation Engineering
Chinese University of Hong Kong, Hong Kong

DOI: 10.1002/aenm.201601248

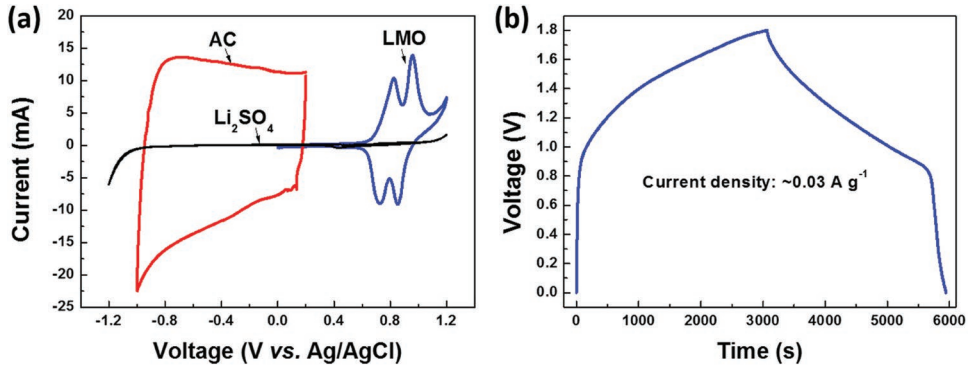

Figure 1. a) Cyclic voltammogram plots of LMO solid electrode (0.0–1.2 V, 0.5 mV s^{-1}), 1 M Li_2SO_4 electrolyte (–1.2 to 1.2 V, 0.5 mV s^{-1}) and AC solid electrode (–1.0 to 0.2 V, 2.0 mV s^{-1}). b) Charging/discharging profiles of the LMO/AC aqueous Li-ion capacitor at current density of ≈0.03 A g^{-1} (based on the mass of both LMO and AC active materials) in the voltage range of 0.0–1.8 V.

2. Results and Discussion

2.1. Electrochemical Properties of Conventional LMO and AC Solid Electrodes

The electrochemical stability of the 1 M Li_2SO_4 aqueous electrolyte was first evaluated using cyclic voltammetry (CV) at a scan rate of 0.5 mV s^{-1} between –1.2 and 1.2 V versus Ag/AgCl reference electrode. It was found that the Li_2SO_4 electrolyte was stable in the voltage range of –1.0 to 1.0 V versus Ag/AgCl reference electrode (**Figure 1**a). In contrast, the LMO sample exhibited two typical oxidation/reduction peaks at 0.82 V/0.73 V and 0.96 V/0.85 V versus Ag/AgCl reference electrode during the anodic/cathodic scan, indicating a two-step reaction for Li ions extraction/insertion in LMO material. The phase changes during the CV scan were disclosed by ex-situ X-ray diffraction (XRD) performed at a few representative voltage stages during the anodic and the cathodic scan (Figure S1, Supporting Information). Phase transitions from cubic phases of $LiMn_2O_4$ to $Li_xMn_2O_4$, and to λ-MnO_2 in the anodic scan, and the reversed transitions in the cathodic scan were observed, corresponding to the delithiation and lithiation processes. These results were consistent with literature reports.[10] In addition, O_2 evolution occurred at ≈1.0 V versus Ag/AgCl reference electrode in the CV scan of LMO conventional solid electrode (Figure 1a). Because of the high overpotential of O_2 evolution on the LMO surface (>1.1 V vs Ag/AgCl reference electrode), the O_2 was mainly generated on the surface of carbon additive which was introduced to LMO solid electrode to improve the electronic conductivity.[11] The first charging and discharging capacities cycled at current density of 0.4 A g^{-1} in the voltage range of 0.0–1.0 V versus Ag/AgCl reference electrode were 83.2 mA h g^{-1}, and 69.3 mA h g^{-1}, respectively (Figure S2a, Supporting Information), corresponding to an initial coulombic efficiency of ≈83.2%. Nevertheless, the coulombic efficiency increased to >96.0% afterward (>10 charging/discharging cycles, Figure S2b, Supporting Information). The relatively low coulombic efficiencies mainly resulted from the O_2 evolution on the surfaces of the carbon additive.[11] This problem may be alleviated by engineering the carbon additives in the future.

The CV of AC solid electrode exhibited a typical rectangular profile in the voltage range of –1.0 to 0.2 V versus Ag/AgCl reference electrode (Figure 1a), corresponding to the reversible absorption/desorption of Li ions on the AC electrode. The specific capacitances of the AC electrode were evaluated using CV at different scan rates in the voltage range of –1.0 to 0.2 V versus Ag/AgCl reference electrode, which results were summarized in Figure S3 (Supporting Information). For example, the specific capacitance was 142.1 F g^{-1} at scan rate of 2.0 mV s^{-1}.

The capacitor characteristics of the aqueous solid Li-ion capacitor were evaluated by coin cell consisting of LMO positive electrode and AC negative electrode (LMO/AC). In order to maximize the energy density of this system, the mass ratio between the LMO and AC was adjusted to ≈1:1.5 by considering the specific capacities/capacitances of the individual electrodes.[11] Figure 1b showed the charging/discharging profiles of the LMO/AC aqueous Li-ion capacitor at current density of ≈0.03 A g^{-1} of active materials between 0.0 and 1.8 V. The corresponding discharging specific capacitance was ≈52.3 F g^{-1} based on total mass of the LMO and AC active materials. The cell exhibited a sloping voltage profile in the voltage range of 0.8–1.8 V, delivering a maximized energy density of ≈31 W h kg^{-1}.

2.2. Characterizations and Electrochemical Properties of LMO and AC Slurry Electrodes

Three samples of LMO slurries were prepared with 10 wt% LMO and 2.0, 2.5, or 4.0 wt% Ketjen black (KB). The corresponding slurries were denoted as L10K2, L10K2.5, and L10K4. In order to investigate their morphologies and compositions, the LMO slurries were dried and characterized using a scanning electron microscope. The typical results were shown in **Figure 2**a–d (obtained using sample L10K4). Particles in the size of micrometers can be observed (Figure 2a). The high contrast regions in the backscattering electron image in Figure 2b suggested the presence of heavy elements, which should originate from the LMO particles. The LMO particles were uniformly dispersed in carbon matrix, as revealed by the elemental maps of Mn and C (Figure 2c,d).

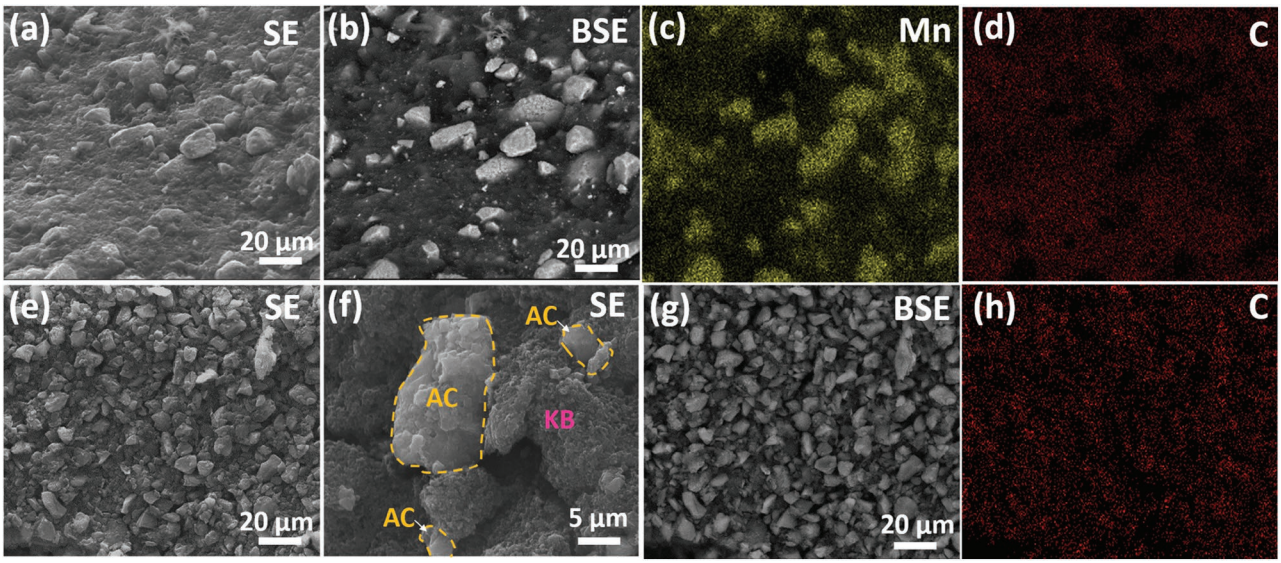

Figure 2. SEM images of L10K4 dry slurry taken with a) secondary electrons (SE) and b) backscattering electrons (BSE). EDX elemental mapping of c) Mn and d) C taken from the same region shown in (a). SEM images of A20K2 dry slurry taken at e,f) SE and g) BSE mode. h) C elemental mapping taken from the same region shown in (e).

Two samples of AC slurries were prepared with 10 wt% AC and 1 or 2 wt% KB, being denoted as A20K1 and A20K2, respectively. The morphologies of the AC slurry samples were similar, and Figure 2e–h showed the results taken from the A20K2 slurry. The size of AC particles was in the range of ≈5 to ≈15 μm, and these particles were connected with KB (Figure 2f). Furthermore, the different structures of AC (dense particle) and KB (hollow structure) led to different contrasts in the backscattering electron image (Figure 2g) and elemental map of C (Figure 2h), which revealed the formation of uniform mixture of AC and KB.

The impact of KB content on the electrical properties of the semi-solid slurry was investigated. The electronic and ionic conductivities of the LMO slurries with different KB content (2.0, 2.5, and 4.0 wt%) were determined using alternating current method.[12] The Nyquist plots of the three samples were shown in **Figure 3**a. A semicircle at high frequency region represented interfacial resistance resulting from the contact between the semi-solid slurries and the current collector. The following semicircle at lower frequency region comes from the parallel combination of both the ionic and electronic resistances due to the ion displacement and the electron flow in the percolated network.[12b] An appropriate equivalent circuit model (inset of Figure 3a) was established to fit the Nyquist curves, and key parameters characteristic of the slurries' electrical properties were estimated, as shown in Figure 3b. The ionic conductivities of the slurries were in the range of 51.6–59.8 mS cm^{-1}, which appeared to be independent of the KB content but relied on the aqueous electrolyte employed (ionic conductivity of 1 M Li_2SO_4 aqueous solution: ≈60 mS cm^{-1}[13]). In contrast, the electronic conductivities increased from 1.5, to 4.7, and to 46.2 mS cm^{-1} for the L10K2, L10K2.5, and L10K4 slurries (intrinsic electrical conductivity of LMO: ≈0.019 mS cm^{-1}[14]), revealing the critical function of KB in the slurry, i.e., serving as percolated network for electron flow. These results indicated that the conductivity of the slurry was mainly limited by its electronic conductivity. In addition, the interfacial resistance resulting from the slurry/current collector interfaces also decreased largely with the increase of the KB content. We also compared the electronic conductivities of the LMO slurry samples with either carbon or gold being employed as the current collector, and similar results were obtained, that is, the electrical properties of the LMO slurries did not rely much on the employment of carbon current collectors in the present work (Figure S4, Supporting Information).

The electrical properties of the AC slurries were estimated using similar method (Figure 3c,d). The ionic conductivities were estimated as ≈54–59 mS cm^{-1}, similar to that of the LMO slurries. The electronic conductivity of the A20K1 was estimated as ≈0.6 mS cm^{-1} (intrinsic electrical conductivity of AC: ≈500–2100 mS cm^{-1}[15]), which was much lower than that of the A20K2 (≈9.5 mS cm^{-1}). These results revealed the critical function of KB in the slurry again. Furthermore, the interfacial resistance also greatly decreased with the increase of the KB content. We therefore used A20K2 slurry as semi-solid anode to pair with the L10K2.5 or L10K4 slurries in respective studies shown below.

The rheological behaviors of the prepared slurries were measured whose results are shown in **Figure 4**. In general, all the slurries exhibited strong shear-thinning behavior, i.e., the viscosity decreased with the increase of shear strain. In addition, the viscosities of these slurries were greatly dependent on the fraction of the solid phase, especially the content of KB which was of low density. Higher mass fraction of KB occupied larger volume in the slurries, leading to higher viscosities of the corresponding slurries. For example, the L10K4 (KB volume fraction of ≈28 vol%) exhibited much higher viscosity as compared to the L10K2.5 (KB ≈19 vol%) and L10K2 (KB ≈16 vol%).

The specific capacities of the LMO slurries were determined using three-electrode system in which the LMO slurries, overweight AC solid electrode, and a chloride silver foil

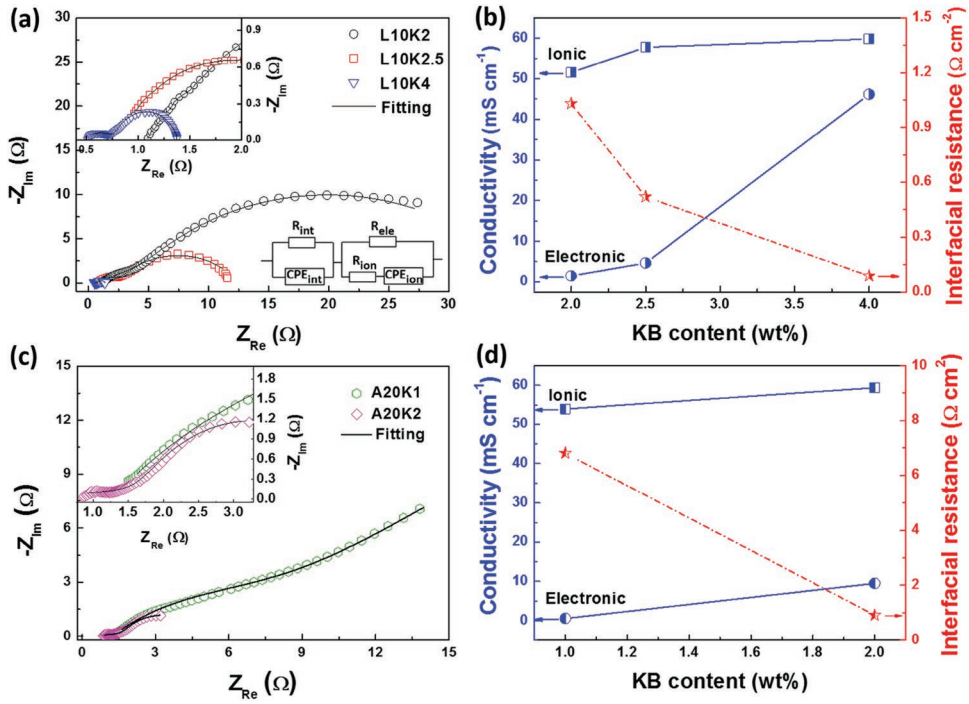

Figure 3. a) Nyquist plots of the LMO slurries with different KB content. The inset showed the equivalent circuit model for these plots. R_{int} and CPE_{int} stood for interfacial resistance and capacitance at the slurry/current collector interfaces. R_{ion} and CPE_{ion} represented ionic resistance and double layer capacitance of suspended electrode surfaces, respectively. R_{ele} represented electronic resistance of the slurries. The lines in Figure 2a were the fitted curves by using this equivalent model. b) Electronic, ionic conductivity and interfacial resistance of the LMO slurries with different KB content. c) Nyquist plots of A20K1 and A20K2 slurries. d) Electronic, ionic conductivity and interfacial resistance of these two slurries.

were used as the working electrode, the counter electrode, and the reference electrode. **Figure 5**a shows charging/discharging curves of the L10K4 slurry tested at various current densities in the voltage range of 0.0–1.0 V versus Ag/AgCl reference electrode. The current density values are in the unit of mA cm^{-2} which is conventionally adopted for flow batteries and flow capacitors. The nonlinear change of the voltage profiles indicates the occurrence of non-faradic reaction during the charging/discharging processes. The duration of charging/discharging procedure decreased gradually with the increase in current densities, which was mainly attributed to the insufficient extraction/insertion of Li ions during the charging/discharging processes. The rate performance of the L10K4 slurry is shown in Figure 5b. The specific capacities of the slurries were calculated based on the mass of LMO active material. At low current density of 1.0 mA cm^{-2} (≈0.13 A g^{-1} considering LMO mass only), these slurries delivered the specific capacity of ≈73.2 mA h g^{-1}, which was similar to that of the LMO solid electrode. When the current density increased to 10.0 mA cm^{-2} (≈1.25 A g^{-1} considering LMO mass only), the specific capacity of the slurry decreased to ≈20.6 mA h g^{-1}. The rate performance of the LMO slurry electrode was comparable to other semi-solid electrode systems.[3b,16]

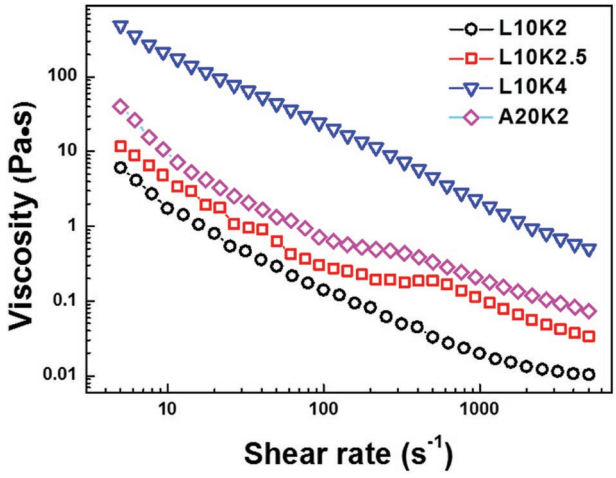

Figure 4. Viscosity versus shear rate for the LMO and AC slurries.

Furthermore, the electrochemical performances of the A20K2 slurry were also investigated. Figure 5c showed the cyclic voltammograms of the A20K2 slurry measured at various scan rates in the voltage range of −1.0 to 0.0 V versus Ag/AgCl reference electrode. These approximately rectangular shaped curves were the typical characteristic of double layer capacitance of the carbon electrode, corresponding to the reversible absorption/desorption of Li ions on the AC surface. Thus, the specific capacitances at different scan rates can be obtained from these cyclic voltammograms whose results are shown in Figure 5d. At low scan rate of 2 mV s^{-1}, the specific capacitance is 112.6 F g^{-1}, which was lower than that of the AC solid electrode (142.1 F g^{-1} at scan rate of 2 mV s^{-1}).

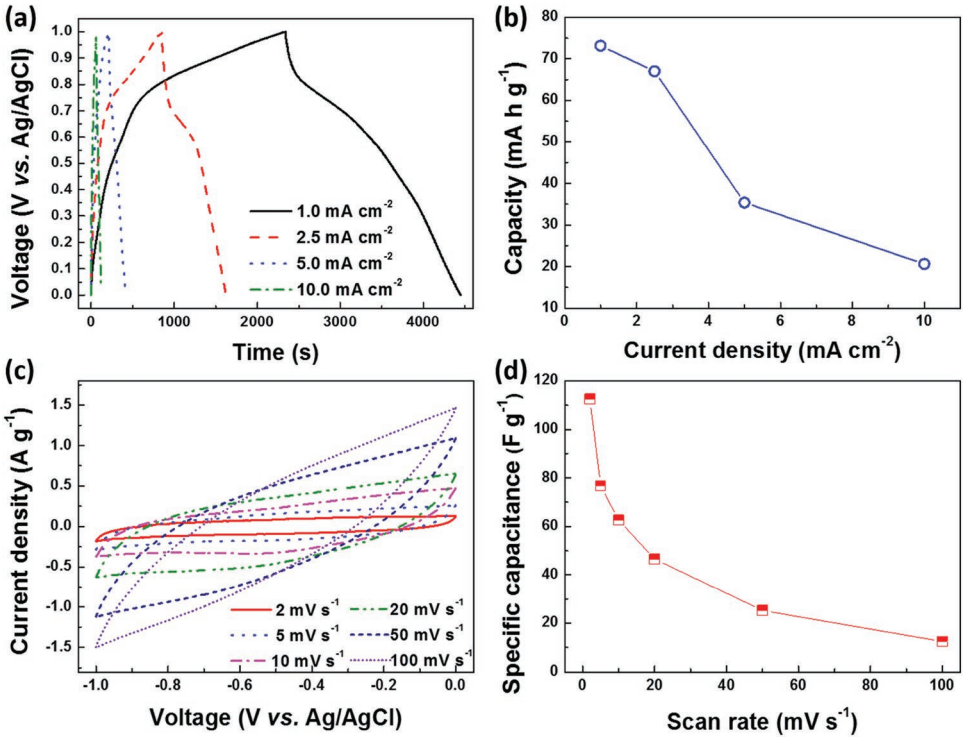

Figure 5. a) Charging/discharging curves of the L10K4 slurries tested at various current densities in the voltage range of 0.0–1.0 V versus Ag/AgCl reference electrode. b) Rate performances of this slurry electrode. c) Cyclic voltammograms of the A20K2 slurry tested at various scan rates in the voltage range of −1.0 to 0.0 V versus Ag/AgCl reference electrode. d) Specific capacitances or capacities of this slurry at different scan rates.

2.3. Electrochemical Properties of LMO/AC Flow Li-Ion Capacitor Tested at Static Condition

In order to evaluate the electrochemical properties of the full cell of the Li-ion flow capacitor, the LMO slurries and AC slurries were matched using a static two-electrode configuration, in which they served as the catholyte and anolyte, respectively. The charging/discharging profiles of the L10K4/A20K2 static cell tested at different current densities in the voltage range of 0.0–1.8 V were shown in **Figure 6**a. The specific capacitances and volumetric capacitances (based on the total mass of LMO and AC or total volume of both slurry electrodes) were calculated, as shown in Figure 6b. At a current density of 2.5 mA cm^{-2} (≈0.09 A g^{-1} considering total mass of LMO and AC in the slurries), the Li-ion flow capacitor delivered a specific capacitance of 52.0 F g^{-1} or a volumetric capacitance of 25.1 F mL^{-1}, corresponding to an energy density of 23.4 W h g^{-1} or 11.4 W h L^{-1}, respectively. When the current density was increased to 15.0 mA cm^{-2} (≈0.53 A g^{-1}), the specific and the volumetric capacitances can still be maintained at 21.3 F g^{-1} (energy density of 9.6 W h g^{-1}) and 6.2 F mL^{-1} (energy density of 2.8 W h L^{-1}), respectively. On the other hand, the LMO/AC Li-ion flow capacitor exhibited excellent cycling performance. For example, the L10K4/A20K2 static cell tested at a current density of 10.0 mA cm^{-2} (≈0.35 A g^{-1}) delivered remarkably stable discharge capacitance of ≈30 F g^{-1} with a high coulombic efficiency of ≈99.2% during 1000 charging/discharging cycles (Figure 6c).

Figure 6d gave the Ragone plot of the L10K4/A20K2 Li-ion flow capacitor. Its energy density reached 23.4 W h kg^{-1} at a power rate of 50.0 W kg^{-1}, and decreased to 10.7 W h kg^{-1} at a power of 490.9 W kg^{-1}. The energy and power densities of several other reported aqueous flow capacitors in the literature were also presented in the same Ragone plot. All reference data from the literature were obtained at static condition. It was shown that the aqueous Li-ion capacitor can deliver ≈1.5–5 times higher energy density than those of other counterparts, including the aqueous symmetric devices based on reduced graphene oxide-wrapped carbon spheres (rGO-CS),[10a] optimized activated carbon spheres (AC1000/aq.),[10b] activated carbon sphere coexisting with redox-active hydroquinone (CS-0.3M HQ, CS-0.08M HQ),[3b] and aqueous asymmetric devices such as MnO_2/activated carbon (MnO_2/AC)[4] flow capacitor. The energy densities of the LMO/AC aqueous Li-ion flow capacitor in the present study were actually comparable to that of the symmetric flow capacitor using organic electrolyte, for which the voltage window was expanded to 2.5 V due to the employment of organic electrolyte (greatly undesired due to safety concern and system cost[9c]). Furthermore, this aqueous Li-ion flow capacitor exhibited much higher power densities as compared to conventional redox flow batteries.

2.4. Electrochemical Properties of LMO/AC Li-Ion Flow Capacitor Tested at Intermittent-Flow Condition

The LMO/AC slurries were also tested under intermittent-flow condition, in which slugs of LMO and AC slurries were simultaneously injected (flow rate 2 mL min^{-1}) into the flow cell for charging and discharging tests (**Figure 7**a,b). For this purpose,

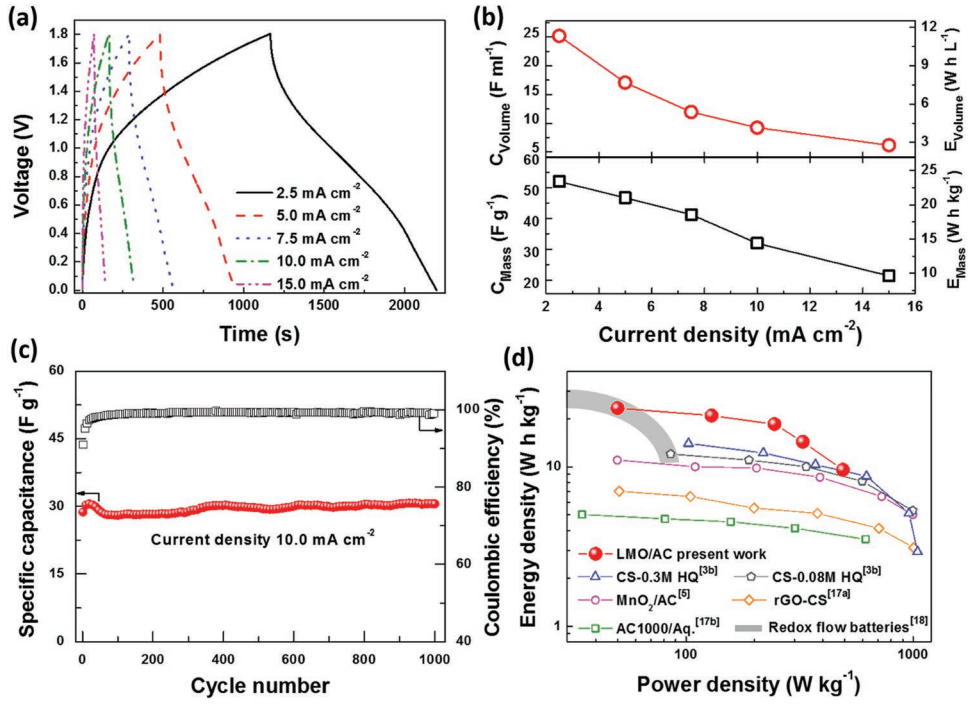

Figure 6. a) Charging/discharging profiles of the L10K4/A20K2 static cell tested at different current densities in the voltage range of 0.0–1.8 V. b) Specific capacitances (C_{Mass}) and volumetric capacitances (C_{Volume}) of this static cell obtained at different current densities. The corresponding energy densities were also given. c) Long cycling performance of this cell tested at a current density of 10.0 mA cm^{-2} (≈0.35 A g^{-1}). d) Ragone plot of the L10K4/A20K2 flow Li-ion capacitor and the comparison with other type of flow capacitors tested at static condition.[3b,5,17] A common performance of conventional redox flow batteries is also shown in (d).[18]

the L10K2.5 slurry was employed as the catholyte to match with the A20K2 anolyte due to its better flowability. Figure 7c presented the charging and discharging curves for four iterations of injection of the L10K2.5/A20K2 flow Li-ion capacitor tested at a current density of 2.5 mA cm^{-2} (≈0.09 A g^{-1}). The charging/discharging energy densities of these four slugs were 22.6/21.2, 24.0/18.6, 19.6/15.7, and 20.9/19.8 W h kg^{-1}, corresponding to energy efficiencies of 93.5%, 77.4%,79.8%,

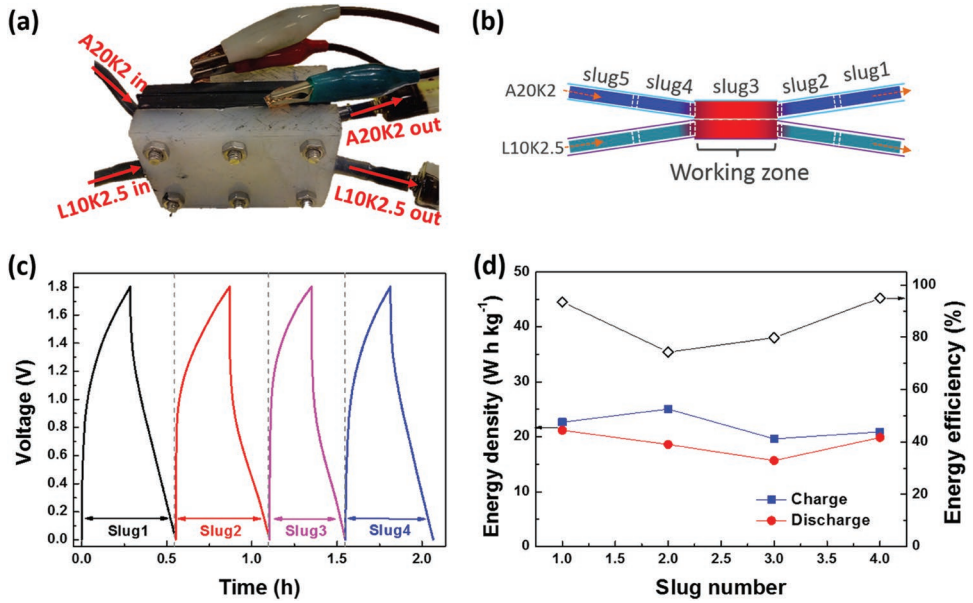

Figure 7. a) Photograph of flow cell configuration. b) Schematic of intermittent-flow tests of L10K2.5/A20K2 flow Li-ion capacitor. c) Charging and discharging curves for four iterations of injection of the flow Li-ion capacitor tested at current density of 2.5 mA cm^{-2} (≈0.09 A g^{-1}). d) Energy densities and energy efficiencies of the Li-ion flow capacitor under the intermittent-flow condition.

and 95.0% (Figure 7d). The instability of the energy densities likely came from some in the pumped volume, which was also observed in the intermittent-flow tests of semi-solid flow battery.[19] The results in Figure 7 represented the first demonstration of a full operational hybrid Li-ion flow capacitor.

3. Conclusion

Taking advantage of high capacity of Li-ion batteries, high power density, and long life of supercapacitors and the scalability of flow batteries, we demonstrated high energy and power density aqueous Li-ion hybrid flow capacitors with long cycle life using $LiMn_2O_4$ and activated carbon slurry electrodes. Compared to the existing aqueous flow electrochemical capacitor systems, the Li-ion hybrid flow capacitor exhibited remarkably high energy densities due to the introduction of high-performance Li-insertion-type electrode materials (e.g., $LiMn_2O_4$ in the present work) as the flowable slurry electrode, which contributed to both high capacity and large working voltage window (resulted from the asymmetrical configuration with AC as the other electrode). A record energy density (23.4 W h kg^{-1} at a power of 50.0 W kg^{-1}) had been achieved for aqueous flow capacitors tested at static condition reported to date. Analyses of electrical properties of the slurries suggested the importance of the KB content, which determined the transport of electrons in the slurries. A full operational Li-ion flow capacitor tested in an intermittent-flow mode was also demonstrated. The Li-ion hybrid flow capacitor showed promise for large-scale electrochemical energy storage.

4. Experimental Section

Synthesis of Conventional Solid Electrodes and Slurry Electrodes: To fabricate LMO or AC conventional solid electrodes, 80 wt% commercial LMO powder or AC (Shen Zhen Kejing Star Ltd., China), 10 wt% Ketjen black (ECP600JD), 10 wt% of polyvinylidene fluoride (PVDF) binder, and moderate *N*-methyl-2-pyrrolidone (NMP) solvent were mixed and pasted on Ni foam current collector. Then the NMP solvent was removed using vacuum drying at 120 °C. The final solid electrodes were pressed flat under a pressure of 10 MPa cm^{-2}. The corresponding slurry electrodes were prepared by mixing active materials (LMO or AC), Ketjen black, and Li_2SO_4 (1 M) aqueous solution. In LMO slurries, the mass ratios of LMO were kept at 10 wt%, matching with different mass ratio of Ketjen black of 2.0, 2.5, or 4.0 wt% (denoted as L10K2, L10K2.5, and L10K4, respectively). The AC slurries consisted of 10 wt% AC and 1 or 2 wt% Ketjen black (denoted as A20K1 and A20K2).

Characterizations: The morphologies and compositions of the samples, prepared from slurries with electrolyte removed, were characterized by a field emission scanning electron microscope (FESEM, Quanta 200, FEI). Rheological measurements were carried out on a stress-controlled rheometer (Physica MCR301, Anton Paar) using a plate-plate geometry (plate diameter 40 mm, gap 0.049 mm) at room temperature. The shear rate was increased from 5 to 5000 s^{-1} during each test.

Electrical Properties of the Flow Li-Ion Capacitors: The electrochemical properties of LMO or AC conventional solid electrodes, for example, charging/discharging profiles and cyclic voltammograms, were performed using an electrochemical working station (CHI 660C, Shanghai Chenhua Instrument Co., Ltd.) with three-electrode configuration, in which LMO or AC solid electrodes, Pt foil, and Ag/AgCl electrode were used as the working, the counter, and the reference electrode. The full cells were examined using CR2032 coin cell with LMO and AC conventional solid electrodes as the positive and negative electrode. The electrochemical testing was performed using BTS batteries testing system (CT4008W, Neware Co., Ltd.). For the electrochemical tests of the slurries, a self-made cell which consisted of two carbon plate current collectors separated by two gaskets (thickness of 1 mm) was fabricated. A groove with an active area of 40×5 mm^2 as flow channel was made in each gasket. A Celgard 3501 film was clamped by these two gaskets as separator. A single channel configuration without Celgard separator was used for the electrochemical impedance spectroscopy (EIS) tests of the slurries. The EIS of the slurries was measured in the frequency range from 100 kHz to 0.05 Hz under an alternating current stimulus with a 10 mV of amplitude (CHI 660C). The electrochemical properties of LMO (or AC) single slurry were characterized using the above self-made cell with three-electrode configuration, in which LMO (or AC slurry), overweight AC solid electrode, and a chloride silver foil were used as the working, the counter, and the reference electrode. During electrochemical tests of full cell of the LMO/AC slurries, the self-made cell with two channels configuration was employed at static and intermittent mode. In the intermittent mode, the slurries were pumped using a dual-channel syringe pump (LSP02-1, Baoding Longer Precision Pump Co., Ltd.).

Supporting Information

Supporting Information is available from the Wiley Online Library or from the author.

Acknowledgements

H.L. acknowledges the support from the National Natural Science Foundation of China (No. 51502271) and the Fundamental Research Funds for the Central Universities (No. 2652015186). Q.L. acknowledges the support from the National Natural Science Foundation of China/Research Grants Council Joint Research Scheme (No. N_CUHK448/13).

Received: June 11, 2016
Revised: August 18, 2016
Published online: September 20, 2016

[1] V. Presser, C. R. Dennison, J. Campos, K. W. Knehr, E. C. Kumbur, Y. Gogotsi, *Adv. Energy Mater.* **2012**, *2*, 895.
[2] G. L. Soloveichik, *Chem. Rev.* **2015**, *115*, 11533.
[3] a) M. Boota, K. B. Hatzell, E. C. Kumbur, Y. Gogotsi, *ChemSusChem* **2015**, *8*, 835; b) H. Yoon, H.-J. Kim, J. J. Yoo, C.-Y. Yoo, J. H. Park, Y. A. Lee, W. K. Cho, Y.-K. Han, D. H. Kim, *J. Mater. Chem. A* **2015**, *3*, 23323; c) K. B. Hatzell, M. Beidaghi, J. W. Campos, C. R. Dennison, E. C. Kumbur, Y. Gogotsi, *Electrochim. Acta* **2013**, *111*, 888.
[4] K. B. Hatzell, M. Boota, E. C. Kumbur, Y. Gogotsi, *J. Electrochem. Soc.* **2015**, *162*, A5007.
[5] K. B. Hatzell, L. Fan, M. Beidaghi, M. Boota, E. Pomerantseva, E. C. Kumbur, Y. Gogotsi, *ACS Appl. Mater. Interfaces* **2014**, *6*, 8886.
[6] S. Sasi, A. Murali, S. V. Nair, A. S. Nair, K. R. V. Subramanian, *J. Mater. Chem. A* **2015**, *3*, 2717.
[7] a) V. Aravindan, J. Gnanaraj, Y.-S. Lee, S. Madhavi, *Chem. Rev.* **2014**, *114*, 11619; b) H. Kim, K.-Y. Park, M.-Y. Cho, M.-H. Kim, J. Hong, S.-K. Jung, K. C. Roh, K. Kang, *ChemElectroChem* **2014**, *1*, 125; c) Y.-G. Wang, Y.-Y. Xia, *J. Electrochem. Soc.* **2006**, *153*, A450.
[8] a) Y.-G. Wang, J.-Y. Luo, C.-X. Wang, Y.-Y. Xia, *J. Electrochem. Soc.* **2006**, *153*, A1425; b) J.-L. Liu, L.-Z. Fan, X. Qu, *Electrochim. Acta* **2012**, *66*, 302.
[9] a) W. Tang, Y. Zhu, Y. Hou, L. Liu, Y. Wu, K. P. Loh, H. Zhang, K. Zhu, *Energy Environ. Sci.* **2013**, *6*, 2093; b) W. Tang, Y. Hou,

F. Wang, L. Liu, Y. Wu, K. Zhu, *Nano Lett.* **2013**, *13*, 2036; c) Y. G. Wang, J. Yi, Y. Y. Xia, *Adv. Energy Mater.* **2012**, *2*, 830.
[10] a) M. N. Richard, I. Koetschau, J. R. Dahn, *J. Electrochem. Soc.* **1997**, *144*, 554; b) J. Yan, J. Wang, H. Liu, Z. Bakenov, D. Gosselink, P. Chen, *J. Power Sources* **2012**, *216*, 222.
[11] Y.-G. Wang, Y.-Y. Xia, *Electrochem. Commun.* **2005**, *7*, 1138.
[12] a) K. B. Hatzell, M. Boota, Y. Gogotsi, *Chem. Soc. Rev.* **2015**, *47*, 8664; b) M. Youssry, L. Madec, P. Soudan, M. Cerbelaud, D. Guyomard, B. Lestriez, *Phys. Chem. Chem. Phys.* **2013**, *15*, 14476.
[13] K. Fic, G. Lota, M. Meller, E. Frackowiak, *Energy Environ. Sci.* **2012**, *5*, 5842.
[14] S. Chitra, P. Kalyani, T. Mohan, M. Massot, S. Ziolkiewicz, R. Gangandharan, M. Eddrief, C. Julien, *Ionics* **1998**, *4*, 8.
[15] J. Gamby, P. L. Taberna, P. Simon, J. F. Fauvarque, M. Chesneau, *J. Power Sources* **2001**, *101*, 109.
[16] a) L. Madec, M. Youssry, M. Cerbelaud, P. Soudan, D. Guyomard, B. Lestriez, *ChemPlusChem* **2015**, *80*, 396; b) L. Madec, M. Youssry, M. Cerbelaud, P. Soudan, D. Guyomard, B. Lestriez, *J. Electrochem. Soc.* **2014**, *161*, A693.
[17] a) M. Boota, K. B. Hatzell, M. Alhabeb, E. C. Kumbur, Y. Gogotsi, *Carbon* **2015**, *92*, 142; b) M. Boota, K. B. Hatzell, M. Beidaghi, C. R. Dennison, E. C. Kumbur, Y. Gogotsi, *J. Electrochem. Soc.* **2014**, *161*, A1078.
[18] K. Percin, *Master Degree Thesis*, Hacettepe University (Ankara, Turkey), **2015**.
[19] M. Duduta, B. Ho, V. C. Wood, P. Limthongkul, V. E. Brunini, W. C. Carter, Y.-M. Chiang, *Adv. Energy Mater.* **2011**, *1*, 511.

ADVANCED ENERGY MATERIALS

Supporting Information

for *Adv. Energy Mater.,* DOI: 10.1002/aenm.201601248

High Energy Density Aqueous Li-Ion Flow Capacitor

Hao Liu, Libing Liao, Yi-Chun Lu, and Quan Li**

Supporting Information

Title: High Energy Density Aqueous Li-ion Flow Capacitor

*Hao Liu *, Libing Liao, Yi-Chun Lu, and Quan Li **

Table S1. Energy density estimation for various aqueous electrochemical capacitors based on solid active materials only.

System [a]	Practical Capacity (mA h g^{-1})	Average Voltage (V)	Energy Density (W h kg^{-1})	Energy Density (W h L^{-1})
Electric double-layer capacitor				
AC/AC	~40 (AC [b])	0.5	10	20
Aqueous metal oxide-based capacitor				
AC/MnO_2	~55 (MnO_2 [c])	0.9	21	56
Aqueous Li-ion capacitor				
$LiMn_2O_4$/AC	~100 ($LiMn_2O_4$ [b])	1.3	37	87
$LiCoO_2$/AC	~110 ($LiCoO_2$ [b])	1.2	35	74

[a] Density of AC, MnO_2, $LiMn_2O_4$ and $LiCoO_2$: 2.0, 5.0, 4.3, and 5.0 g cm^{-3}; [b),c)] The practical capacities of these active materials estimated from references [1] and [2], respectively.

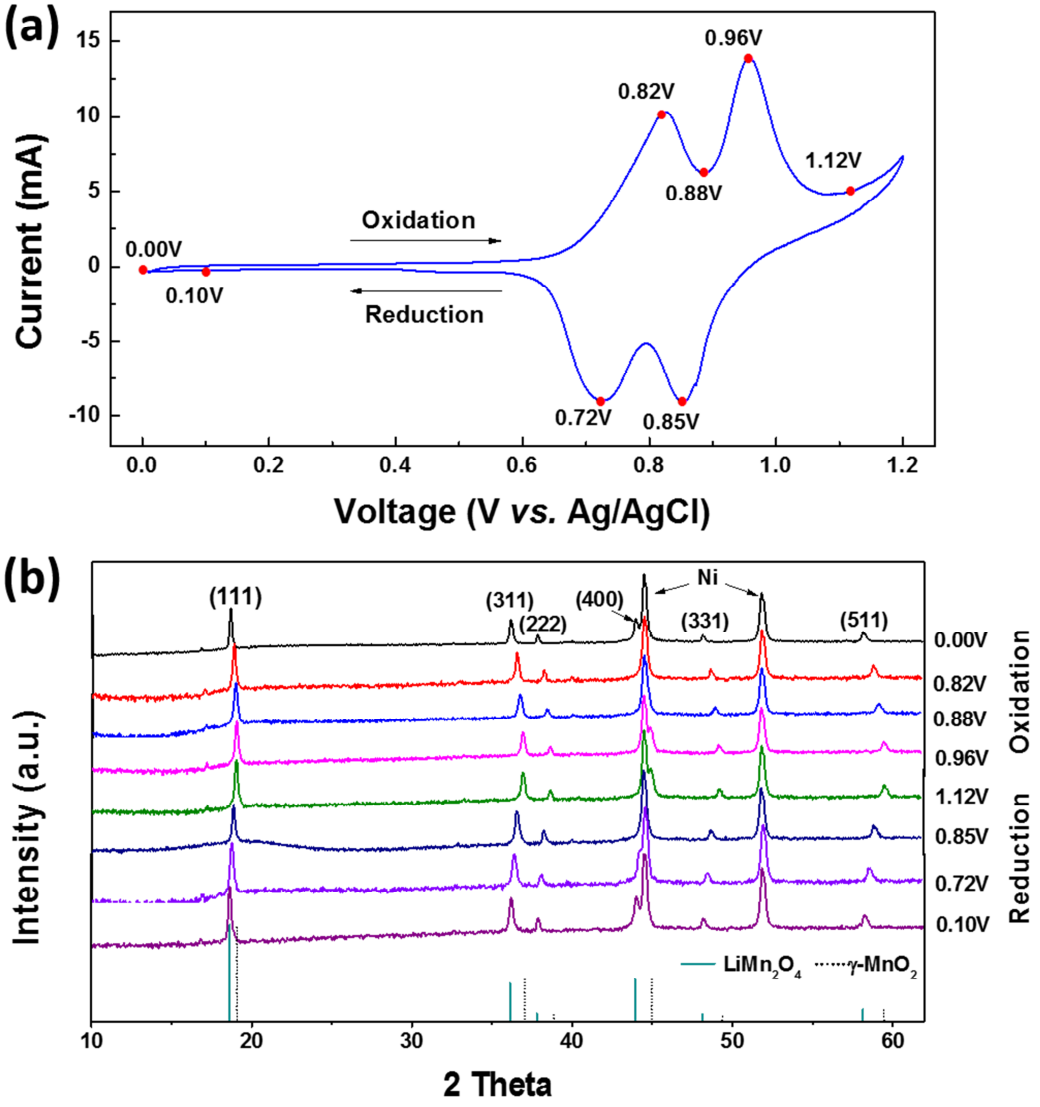

Figure S1. (a) Cyclic voltammogram plot of LMO solid electrode in the voltage range of 0.0~1.2 V *vs.* Ag/AgCl reference electrode at a scan rate of 0.5 mV s^{-1}. (b) XRD patterns taken from the solid electrode at different voltage stages during the CV scan.

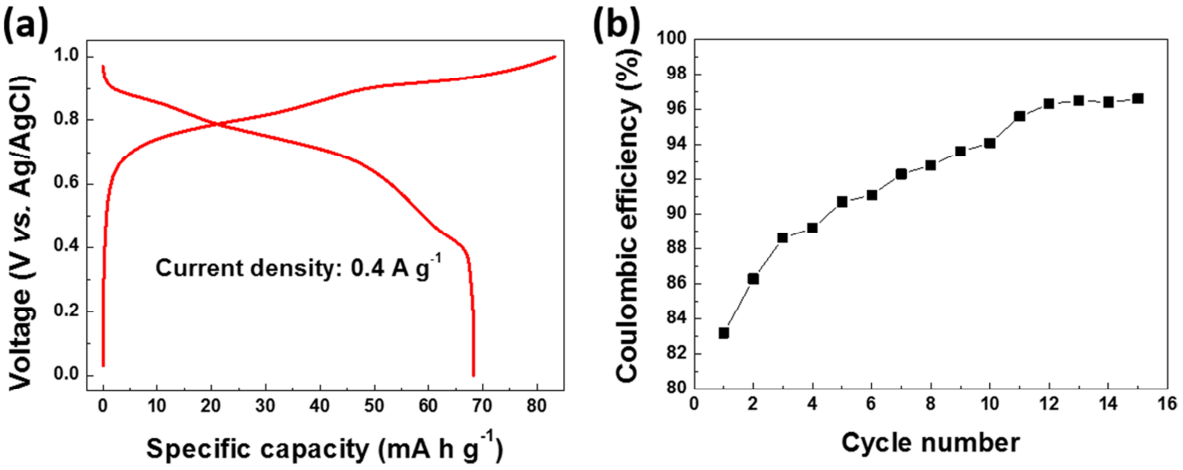

Figure S2. (a) Charge/discharge profiles of the LMO solid electrode cycled at current density of 0.4 A g^{-1} in the voltage range of 0.0 V~1.0 V *vs.* Ag/AgCl reference electrode. (b) Coulombic efficiencies of this electrode during several cycles.

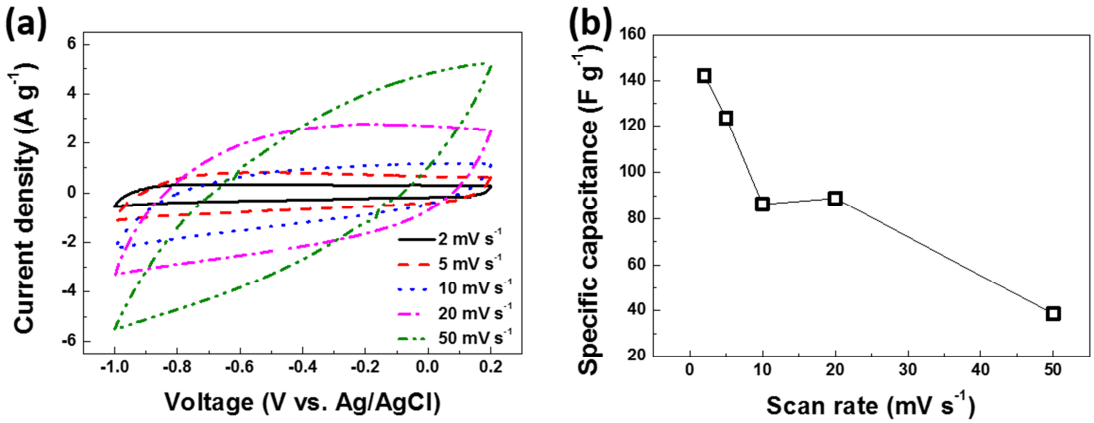

Figure S3. (a) Cyclic voltammogram of the AC solid electrode at various scan rates in the voltage range of -1.0 V~0.2 V *vs.* Ag/AgCl reference electrode. (b) Specific capacitances of the same electrode at different scan rates.

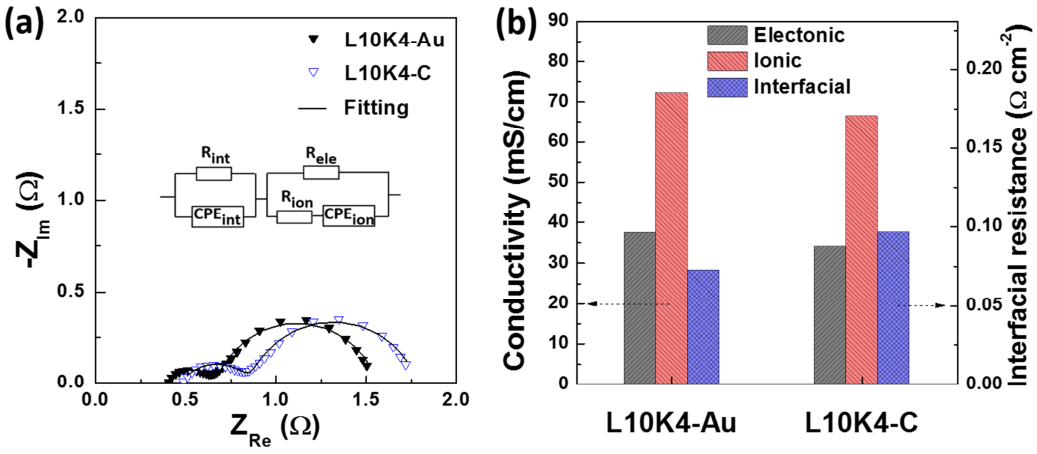

Figure S4. (a) Nyquist plots of the L10K4 slurries with carbon (L10K4-C) or gold (L10K4-Au) current collector. The inset shows the equivalent circuit model for these plots. R_{int} and CPE_{int} stand for interfacial resistance and capacitance at the slurry/current collector interfaces. R_{ion} and CPE_{ion} represent ionic resistance and double layer capacitance of suspended electrode surfaces, respectively. R_{ele} represents electronic resistance of the slurries. The lines in Figure S4a are the fitted curves by using the equivalent model. (b) Electronic, ionic conductivity and interfacial resistance of this slurry with different current collectors.

Reference

[1] Y.G. Wang, Y.Y. Xia, *J. Electrochem. Soc.* **2006**, *153*, A450.

[2] J. L. Liu, L. Z. Fan, X. Qu, *Electrochim. Acta* **2012**, *66*, 302.